Nano World Journal

https://doi.org/10.17756/nwj.2023-s2-001

Research Article

Open Access

Effect of Ammonium Sulfate on the Synthesis of Hydroxyapatite from Electric Arc Furnace Slag

Hind Agourrame*, Hassan Ez-zaki, Nacer Khachani and Abdeljebbar Diouri

Faculté des Sciences, Université Mohammed V de Rabat, Avenue Ibn Battouta, BP 1014, Laboratoire de Chimie Appliquée des Matériaux, Rabat, Morocco

***Correspondence to:**
Hind Agourrame
Faculté des Sciences,
Université Mohammed V de Rabat,
Avenue Ibn Battouta, BP 1014,
Laboratoire de Chimie Appliquée des Matériaux,
Rabat, Morocco.
E-mail: hind.agourrame@gmail.com

Received: July 25, 2023
Accepted: September 18, 2023
Published: September 21, 2023

Citation: Agourrame H, Ez-zaki H, Khachani N, Diouri A. 2023. Effect of Ammonium Sulfate on the Synthesis of Hydroxyapatite from Electric Arc Furnace Slag. *NanoWorld J* 9(S2): S1-S5.

Published by United Scientific Group

Abstract

The steelmaking process results in the by-product formation of electric arc furnace slag (EAFS). Slag is recovered at two different stages of the steelmaking process, the first recovery is black and the second is white mainly consisting of SiO_2, Fe_2O_3, MgO, and CaO. Blast furnace slag, as a by-product from manufacturing, served as a cost-effective raw material for preparation of apatite composite. Hydroxyapatite (HAP) has been commonly applied in medical and pharmaceutical field due to its excellent biocompatibility. Besides, it's also widely applied in adsorption process owing to the adsorption feature. The present research focuses black slag from SONASID-Jorf steel in Morocco for preparation of HAP-calcium silicate hydrate. These phases were successfully synthesized by used ammonium sulfate ($(NH_4)_2SO_4$). Using a wet precipitation method with molar ratio of Ca/P = 1.67 by adding H_3PO_4 and NaOH. X-ray diffraction (XRD), Fourier transform infrared (FT-IR) spectroscopy measurement, scanning electron microscopy (SEM) analysis techniques were performed on the samples to characterize the mineralogical and microstructural properties. The characterization of the developed phases indicates the formation of mixtures of dicalcium silicate with phases of gypsum ($CaSO_4.1/2H_2O$) and killalaite ($Ca_6Si_4O_{14}.2H_2O$) in the black slag activated with activator ammonium sulfate. Moreover, indicates the formation of HAP ($Ca_5(PO_4)_3(OH)$) phase synthesized by wet precipitation method. The micrographs obtained by SEM show the morphology of fine porous particles in the form of spherical agglomerates attributed to HAP.

Keywords

Blast furnace slag, Ammonium sulfate, Hydroxyapatite

Introduction

Slag represents one of the industrial wastes of various metal extractions and refining processes. In the specific case of making steels, the slag is generated at 3 different stages of processing and accordingly classified as: blast-furnace slag, electric arc furnace slag and ladle slag [1]. EAFS is a by-product of the steelmaking industry, generated after the melting and the primary acid refining of liquid steel. Its chemical composition is based on its content of calcium, iron, and silicon oxides in a global amount of over 80%, aluminium, magnesium, manganese, and phosphorus oxides are also present [2]. Moreover, the generation of EAFS grew to 18 Mt in Europe in 2016 [3]. Furthermore, the main compounds of EAFS, according to the scientific literature, are single and complex calcium silicates (containing aluminium or magnesium) and single and complex iron-based oxides (containing calcium, magnesium, chromium, manganese among others) which are in a liquid state above 1500 °C, aided by fluxes such as CaF_2, which solidify at under 1200 °C [2]. Microscopically, the surface of steel slag particles shows slightly concave and convex folds, characterized by porous

structures with random distribution of pores and microcracks, and present a large specific surface area with high adsorption and precipitation capacity [4]. Furthermore, EAFS usually has better porosity and the water absorbing property due to flourishing pore structure [5]. Alkali-activated binders are cementitious materials formed by a chemical reaction of an alkaline solution and an amorphous aluminosilicate material that forms materials with binding properties. Usually, alkali-activated binders are produced by using fly ash, metakaolin or blast furnace slag as aluminosilicate material source [6]. Steel slag is an alkaline material, mainly composed of different oxides, including CaO, SiO_2, Fe_2O_3, Al_2O_3, MgO, MnO, and various alkaline substances that can be combined by H_2O water to release OH^- ions [4]. In the production of cements solely based on slag without a Portland cement component, chemical activation is required to initiate the reactions that will lead to the hardening of the material. In general, alkali silicates, hydroxides or their combination are used as alkaline solutions for the activation process of slag, which are referred to as activating solutions [7]. In a recent study, Slag can also be used to formulate non-Portland cement binders consisting of only slag plus an activator, a system called alkali activated slags. Usually strong alkalis, such as NaOH and/or sodium silicate are used as the activators [8]. Recently, activation of slag by near neutral salts has been given relatively less consideration than silicate or hydroxide activation, as their utilisation compromises the early strength development of these binders, and even the initial hardening of the cement can take several days or longer. Although all nitrite, chloride, and sulfate activators could improve the strength of slag at an early age, it seems that the types of nitrites and chlorides have little impact on the development of slag hydration. Sulfate activators with different cations can promote compressive strength and hydration [8]. Sulfate activation of slag, such as occurs in super-sulfated cement, represents another interesting variant for the achievement of environmentally relevant objectives. By avoiding clinker burning, emission of CO_2 will be clearly reduced by using super-sulfated cement. Furthermore, natural resources such as limestone and combustibles required for OPC production are protected [9]. Steel slag is a commercial waste material mainly containing SiO_2, Al_2O_3, and CaO which are the chemical components of zeolite and HAP, respectively. From the steel slag, a HAP–zeolite composite material (HAP–ZE) was successfully synthesized in a one batch system by adding H_3PO_4 and NaOH [10]. It has been reported recently that zeolites and HAP can be simultaneously synthesized from blast furnace slag under hydrothermal conditions. Synthesized zeolites and HAP using blast furnace slag, observing the formation of these phases over time [11]. With the introduction of fluorite tailings into blast furnace slag, the increase of silica and CaF_2 in the parent glass brought better crystallization and diopside phase formation were induced. With respect to thermal behavior of glass, heat treatment of glass with the composition of 40 wt.% of blast furnace slag and 60 wt.% of fluorite tailings resulted in well sintered glass-ceramics with diopside and fluorapatite as the main crystalline phases [12]. Uniform HAP powder was synthesized successfully utilizing waste neutralization slag, which was prepared without the involvement of surfactants or additives other than the three inexpensive reactants required. The optimum conditions for the synthesis of HAP were 120 °C, pH = 11.5, and a hydrothermal reaction time of 1.5 h. The HAP showed its huge potential for wastewater treatment from vanadium recovery industries with the percentage adsorption of fluoride in the raffinate by HAP can reach 99.66%, and the saturated adsorption concentration was 43.64 mg/g [13]. The objective of this study was to synthesize a HAP derived from EAFS by using ammonium sulfate. The synthesis process employed wet precipitation, with a consistent molar ratio of Ca/P = 1.67. Phosphoric acid was utilized as the precipitating agent during the synthesis procedure. The synthesis mechanism was investigated in detail by XRD, SEM, and FT-IR spectroscopy.

Methodology

In this study, the synthesize of HAP-calcium silicate hydrate mixtures phases were carried out using the following procedure. Initially, the EAFS underwent grinding and sieving processes to achieve a consistent particle size. Subsequently, the obtained powder was activated using ammonium sulfate with a solid-to-liquid ratio (S/L) of 2. The activation process took place in a ceramic container at a temperature of 600 °C for a duration of 90 minutes. This sample prepared using ammonium sulfate is named SSB. After that the product cool down and crush it. Afterward, 5.0 g of the fusion product powder was taken and dissolved in 30 ml of 2.0 mol/L H_3PO_4 aqueous solution until homogenized. Once dissolution is completed, aqueous solution was added drop by drop into the above suspension. It should be noted that the Ca/P molar ratio of the suspension was fixed at 1.7, the obtained slurry was vigorously stirred for 2 h at 100 °C, subsequently aged at the same temperature for a certain time without stirring to achieve crystallization. At the end of the process the solid phase was collected by filtration, washed several times with distilled water, and then dried at 80 °C. The samples prepared with the H_3PO_4 are named respectively SSBP.

Results and Discussion

X-ray fluorescence

The chemical composition of the black furnace slag (EAFS) from SONASID-Jorf steel in Morocco used in the present study was investigated by X-ray fluorescence, results are listed in table 1. The slag was mainly composed of CaO, Al_2O_3, MgO, and SiO_2 components.

X-ray diffraction

Figure 1 shows the XRD diagram of the black furnace slag (EAFS). The analyzes show that the main crystallized phases identified in the black slag (SSB) mainly consists of the crystallized phases: ferrous oxide (FeO), magnesium oxide (MgO), dicalcium silicate (Ca_2SiO_4), and fayalite (Fe_2SiO_4). The intensities of the characteristic diffraction peaks of Ca_2SiO_4 are less in the black slag. This is mainly due to the fact that the black slag is not well crystallized on the other hand the black slag which probably contains vitrified or amorphous compounds. Furthermore, the presence of dicalcium silicate (C_2S) is the preferred phase in slag from the observed peak

Table 1: Chemical composition of the black slag sample Sonasid-Jorf.

Oxides	SB (<40µm)
SiO_2	10.62
Al_2O_3	6.37
Fe_2O_3	25.4
CaO	23.88
MgO	5.04
SO_3	0.29
K_2O	0.01
TiO_2	0.50
MnO	3.07
P_2O_5	0.38
SrO	0.083
LOI	23.75

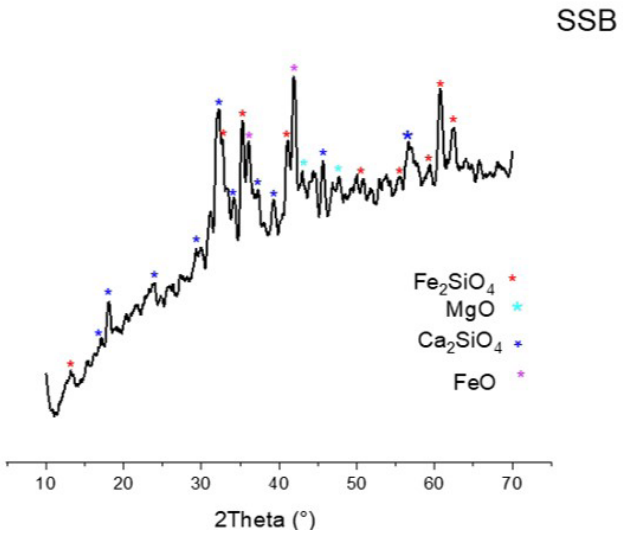

Figure 1: XRD spectra of SSB.

intensity, which shows that the C_2S phase is the main constituent in slag [14].

Figure 2 show the XRD patterns of the black slag activated with ammonium sulfate. The analyzes show that the dicalcium silicate (β-Ca_2SiO_4) phase identified in SSB (Black slag) of the monoclinic crystal system metastable at room temperature [15]. The diffraction pattern shows a mixture of crystalline phases are ferrous oxide (FeO), ferrosilite ($FeSiO_3$), killalaite ($Ca_6Si_4O_{14}.2H_2O$), dicalcium silicate, and gypsum. In figure 2 it can be seen that the hydration products of slag are mainly composed of calcium silicate hydrate phase (C-S-H) like killalaite [16]. The structure crystal of killalaite is monoclinic pseudo cell with a = 6.807, b = 15.459, c = 6.811 Å, β = 97.76°, space group $P2_1/m$, Z = 4, Dx-ray = 2.94 gcm^{-3} [17]. We also note the formation of a crystalline phase corresponding to the ferrosilite ($FeSiO_3$) with space group $P2_1/c$ transforms to a pyroxene with space group $C2/c$ at high pressure [18]. In addition, there is the formation of the gypsum ($CaSO_4.1/2H_2O$) phase. Furthermore, with the appearance of the peaks FeO phase. Figure 2 show the main crystallized phases identified in the SSBP phase are HAP, gypsum, thiosulfate disodium ($Na_2S_2O_3.5H_2O$). The HAP structure was published nearly

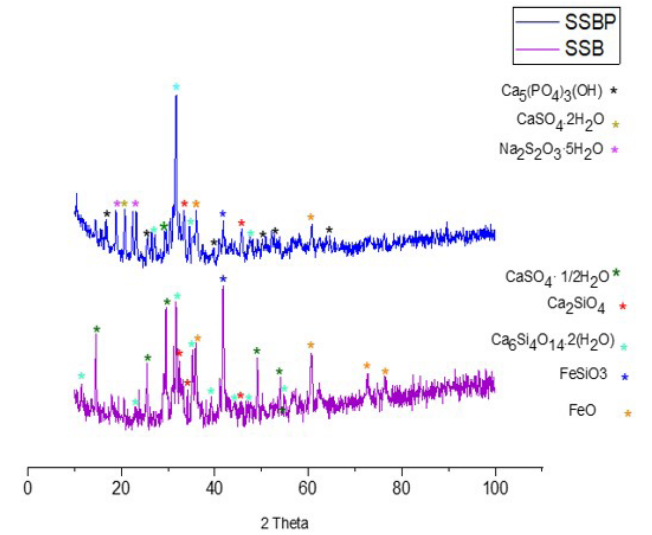

Figure 2: XRD spectra of SSB and SSBP Powders.

simultaneously by Náray-Szabó and Mehmel in 1930. It possesses a hexagonal structure with a $P6_3/m$ space group and cell dimensions a = b = 9.42 Å, and c = 6.88 Å, where $P6_3/m$ refers to a space group with a six-fold symmetry axis with a three-fold helix and a mirror plane, it has an exact stoichiometric Ca/P ratio of 1.67 [19]. Due to the phosphate ions released in reaction remain in the cement matrix until the cement is immersed in water, where they can then react with calcium and phosphate ions released by hydrolysis of tetracalcium phosphate to produce HAP [20]. This latter is a monoclinic structure is the most stable phase at room temperature (25 °C), and the structure has been shown to undergo a reversible phase transition to the hexagonal structure above 200 °C [21].

FT-IR spectroscopy

The FT-IR spectrum of the (SSB-SSBP) powders are presented in figure 3a and 3b. The absorption frequency of the C_2S samples increased in the range of 775 - 400 cm^{-1} [22]. The peaks around 670 cm^{-1} and 602 cm^{-1} are assigned to the stretching and bending of sulfate [23]. The absorption bands located at 1431 cm^{-1} - 1460 cm^{-1} correspond to the Ca-O bond [24]. In the range of O–H stretching vibrations, bands at 3535 cm^{-1} and broad band at 3261 cm^{-1} are distinguished [25]. The MgO nanoparticles were shown IR bands at 451 cm^{-1} are the stretching vibrations of the bond between Mg and O [26]. Furthermore, the stretching bands in 1700 and 750 cm^{-1} wavelengths indicate structural Fe-O vibration [27]. The bands observed in the FT-IR spectra of figure 3b in SSBP phase show the presence of PO_4^{3-} groups can be confirmed

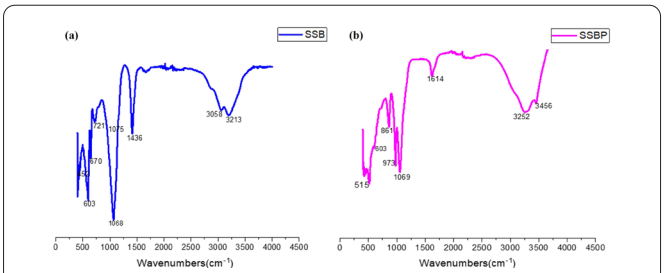

Figure 3: FT-IR Spectrum of **(a)** SSB and **(b)** SSBP powders.

based on the intensive IR absorption bands at 560, 600, and 1000 - 1100 cm^{-1} [28]. The band around 1658 cm^{-1} in the IR spectrum is assigned to the combination of the NH_4 deformation vibration and a H-O-H deformation vibration of the water molecule [29]. Furthermore, to recognize complete apatite formation, the vibrations in the range of 1400 - 900 cm^{-1}, corresponding to the stretching modes of PO_4, were considered as the characteristic peaks of pure apatite [30]. This may be due to the presence of minor impurity of the precursors used during the synthesis process. The absorption bands at, 860 875, and 817 cm^{-1} are contributed to the characteristic absorption peaks of cubic MgO [31]. Furthermore, the notable typical absorption bands at 1053 and 1096 cm^{-1} were assigned to stretching vibration of the phosphate groups [32]. The minor band observed at 3445 cm^{-1} maybe due to the stretching mode of structural OH^- group in HAP [33]. Moreover, the absorption in the interval that extends from 1000 to 1200 cm^{-1} is the signature of the quartz, while the peaks, 3245, 1687, 1621, and 603 cm^{-1} are caused by gypsum [34].

Scanning electron microscopy

SEM (JSM-7000F FE-SEM) is used to study the morphology of samples and obtain information on crystal shape, size, and grain texture. The microstructures of the samples of the SSB phase system are shown in figure 4. They were mainly composed of smooth columnar structures, thin and long fiber structures and aggregated small particles. Moreover, At the same time, the samples had a large number of pores that indicate the presence of crystalline calcium silicate hydrate phase (C-S-H) like killalaite [35]. Figure 4 of SSBP phase shows the heterogeneous surfaces consisting of random-sized particles can be seen. SEM confirmed particles were in the nanoscale but showed the particles were agglomerated [36]. It seems that the agglomerates are HAP nanoparticles agglomerates with round morphology [35]. Furthermore, the HAP nanoparticles formed were highly agglomerated [37, 38].

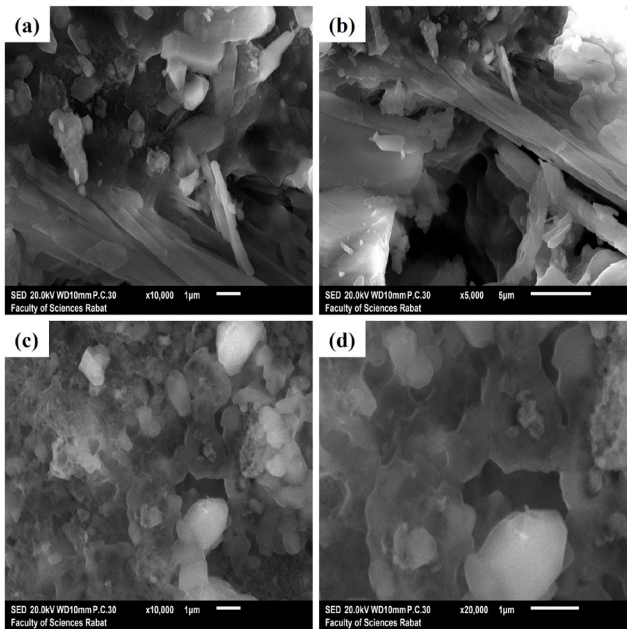

Figure 4: SEM image of SSB sample at **(a)** x10000, **(b)** x5000, and SSBP sample at **(c)** x10000 and **(d)** x20000.

Conclusions

This study reports the effects of ammonium sulfate on the synthesis of HAP from the EAFS, the results of the present study can be summarized as follows:

- The phases ferrosilite, killalaite, and gypsum are identified in the mixture from black slag with activator ammonium sulfate.
- The HAP phase was successfully identified in the mixture.
- Slag activated with the activator ammonium sulfate gives morphological structures with long fibers and aggregates of small size indicating the presence of hydrated phases of crystalline calcium silicate (C-S-H) such as killalaite.
- The use of the wet precipitation method makes it possible to give the agglomerates and the microplates a morphology which is similar to the presence of the HAP phase.

Acknowledgments

None.

Conflict of Interest

None.

References

1. Amin MS, El-Gamal SMA, Abo-El-Enein SA, El-Hosiny FI, Ramadan M. 2015. Physico-chemical characteristics of blended cement pastes containing electric arc furnace slag with and without silica fume. *HBRC J* 11(3): 321-327. https://doi.org/10.1016/j.hbrcj.2014.07.002
2. Arribas I, Santamaría A, Ruiz E, Ortega-López V, Manso JM. 2015. Electric arc furnace slag and its use in hydraulic concrete. *Constr Build Mater* 90: 68-79. https://doi.org/10.1016/j.conbuildmat.2015.05.003
3. Sosa I, Thomas C, Polanco JA, Setién J, Sainz-Aja JA, et al. 2022. Durability of high-performance self-compacted concrete using electric arc furnace slag aggregate and cupola slag powder. *Cement Concr Compos* 127: 104399. https://doi.org/10.1016/j.cemconcomp.2021.104399
4. Shi C, Wang X, Zhou S, Zuo X, Wang C. 2022. Mechanism, application, influencing factors and environmental benefit assessment of steel slag in removing pollutants from water: a review. *J Water Process Eng* 47: 102666. https://doi.org/10.1016/j.jwpe.2022.102666
5. Chen H, Liu Y, Cui H, Zhang W, Hu L, et al. 2022. Effects of electric arc furnace slag on promoting quality and environmental safety of fired bricks incorporating municipal solid waste incineration fly ash. *Constr Build Mater* 345: 128327. https://doi.org/10.1016/j.conbuildmat.2022.128327
6. Siauciunas R, Bankauskaite A, Baltakys K, Stankeviciute M. 2019. The impact of Na_2O on the synthesis of α-C_2SH with different mineral composition and the stability of intermediate and final products. *Ceram Int* 45(2): 2846-2851. https://doi.org/10.1016/j.ceramint.2018.07.291
7. Mobasher N, Bernal SA, Provis JL. 2016. Structural evolution of an alkali sulfate activated slag cement. *J Nuclear Mater* 468: 97-104. https://doi.org/10.1016/j.jnucmat.2015.11.016
8. Rashad AM, Bai Y, Basheer PM, Collier NC, Milestone NB. 2012. Chemical and mechanical stability of sodium sulfate activated slag after exposure to elevated temperature. *Cement Concr Res* 42(2): 333-343. https://doi.org/10.1016/j.cemconres.2011.10.007
9. Matschei T, Bellmann F, Stark J. 2005. Hydration behaviour of sulphate-activated slag cements. *Adv Cement Res* 17(4): 167-178. https://doi.org/10.1680/adcr.2005.17.4.167

10. Kuwahara Y, Ohmichi T, Kamegawa T, Mori K, Yamashita H. 2009. Synthesis of hydroxyapatite–zeolite composite material from disposed steel slag and investigation of its structural and physicochemical characteristics. *Chem Lett* 38(6): 626-627. https://doi.org/10.1246/cl.2009.626

11. Ryu GU, Khalid HR, Lee N, Wang Z, Lee HK. 2020. The effects of NaOH concentration on the hydrothermal synthesis of a hydroxyapatite–zeolite composite using blast furnace slag. *Minerals* 11(1): 21. https://doi.org/10.3390/min11010021

12. Chen J, Yan B, Li H, Li P, Guo H. 2018. Vitrification of blast furnace slag and fluorite tailings for giving diopside-fluorapatite glass-ceramics. *Mater Lett* 218: 309-312. https://doi.org/10.1016/j.matlet.2018.02.020

13. Huang J, Liu T, Zhang Y, Hu P. 2022. Internal coordination of vanadium industrial waste—Preparation of hydroxyapatite and fluorine wastewater purification. *J Water Process Eng* 49: 103041. https://doi.org/10.1016/j.jwpe.2022.103041

14. Chang KL, Huang CT, Huang W, Liu YC. 2008. Investigations of microstructure and phosphorus distribution in BOF slag. *China Steel Tech Rep* 21: 1-6.

15. Dong J, Li C, Liu H, Zhang L, Liu J. 2019. Investigating the mechanical property and reaction mechanism of geopolymers cement with red Pisha Sandstone. *Constr Build Mater* 201: 641-650. https://doi.org/10.1016/j.conbuildmat.2018.12.202

16. Zhang YY, Qi YH, Zou ZS. 2017. Early stage hydration properties of calcium aluminosilicate slag. In 6th International Conference on Advanced Design and Manufacturing Engineering, Zhuhai, China.

17. Taylor HFW. 1977. The crystal structure of killalaite. *Min Mag* 41(319): 363-369. https://doi.org/10.1180/minmag.1977.041.319.08

18. Hugh-Jones DA, Woodland AB, Angel RJ. 1994. The structure of high-pressure C 2/c ferrosilite and crystal chemistry of high-pressure C 2/c pyroxenes. *Am Min* 79(11-12): 1032-1041.

19. Yacoubi AE, Massit A, Moutaoikel SE, Rezzouk A, Idrissi BCE. 2017. Rietveld refinement of the crystal structure of hydroxyapatite using X-ray powder diffraction. *Am J Mater Sci Eng* 5: 1-5. https://doi.org/10.12691/ajmse-5-1-1

20. Matsuya Y, Matsuya S, Antonucci JM, Takagi S, Chow LC, et al. 1999. Effect of powder grinding on hydroxyapatite formation in a polymeric calcium phosphate cement prepared from tetracalcium phosphate and poly (methyl vinyl ether-maleic acid). *Biomaterials* 20(7): 691-697. https://doi.org/10.1016/S0142-9612(98)00231-2

21. da Rocha DN, de Oliveira Cruz LR, de Campos JB, dos Santos JL, Marçal RLSB, et al. 2019. Bioactivity of strontium-monetite coatings for biomedical applications. *Ceram Int* 45(6): 7568-7579. https://doi.org/10.1016/j.ceramint.2019.01.051

22. Wei T, Wei F, Zhou J, Wu Z, Zhang C, et al. 2022. Formation and strengthening mechanisms of xonotlite in C_3S-silica and C_2S-silica powder systems under high temperature and pressure. *Cement Concr Res* 157: 106812. https://doi.org/10.1016/j.cemconres.2022.106812

23. Zhang H, Chai W, Cao Y. 2022. Flotation separation of quartz from gypsum using benzyl quaternary ammonium salt as collector. *Appl Surf Sci* 576: 151834. https://doi.org/10.1016/j.apsusc.2021.151834

24. Nochaiya T, Sekine Y, Choopun S, Chaipanich A. 2015. Microstructure, characterizations, functionality and compressive strength of cement-based materials using zinc oxide nanoparticles as an additive. J *Alloys Compd* 630: 1-10. https://doi.org/10.1016/j.jallcom.2014.11.043

25. Zadov AE, Pekov IV, Zubkova NV, Gazeev VM, Chukanov NV, et al. 2013. Aklimaite, $Ca_4[Si_2O_5(OH)_2](OH)_4.5H_2O$, a new natural hydrosilicate from Mount Lakargi, the Northern Caucasus, Russia. *Geol Ore Deposits* 55(7): 541-548. https://doi.org/10.1134/S1075701513070131

26. Aghel B, Gouran A, Parandi E, Jumeh BH, Nodeh HR. 2022. Production of biodiesel from high acidity waste cooking oil using nano GO@MgO catalyst in a microreactor. *Renew Energy* 200: 294-302. https://doi.org/10.1016/j.renene.2022.09.045

27. Valentín-Reyes J, Coreño O, Nava JL. 2022. Concurrent elimination of arsenic and hydrated silica from natural groundwater by electrocoagulation using iron electrodes. *Chem Eng Res Des* 184: 103-112. https://doi.org/10.1016/j.cherd.2022.05.025

28. Moayedee Y, Mobasherpour I, Banijamali S, Razavi M, Nezafati N. 2022. Effect of the nano-fluorapatite ceramic particles on mechanical behavior of fluoride varnishes. *Mater Chem Phys* 288: 126421. https://doi.org/10.1016/j.matchemphys.2022.126421

29. Culka A, Jehlička J, Němec I. 2009. Raman and infrared spectroscopic study of boussingaultite and nickelboussingaultite. *Spectrochim Acta Part A Mol Biomol Spectrosc* 73(3): 420-423. https://doi.org/10.1016/j.saa.2008.10.026

30. Moayedee Y, Mobasherpour I, Banijamali S, Razavi M, Nezafati N. 2022. Effect of the nano-fluorapatite ceramic particles on mechanical behavior of fluoride varnishes. *Mater Chem Phys* 288: 126421. https://doi.org/10.1016/j.matchemphys.2022.126421

31. Maurya A, Bhatia N. 2017. Microwave assisted sol-gel synthesis of magnesium oxide (MgO). *Int J Eng Res Dev* 13(8): 01-06.

32. Santiago E, Martin V, Colaço B, Fernandes MH, Santos C, et al. 2022. Hydrothermal synthesis of fluorapatite coatings over titanium implants for enhanced osseointegration—an *in vivo* study in the rabbit. *J Funct Biomater* 13(4): 241. https://doi.org/10.3390/jfb13040241

33. Azami M, Jalilifiroozinezhad S, Mozafari M, Rabiee M. 2011. Synthesis and solubility of calcium fluoride/hydroxy-fluorapatite nanocrystals for dental applications. *Ceram Int* 37(6): 2007-2014. https://doi.org/10.1016/j.ceramint.2011.02.025

34. Mechri ML, Chihi S, Mahdadi N, Beddiaf S. 2017. Study of heat effect on the composition of dunes sand of Ouargla (Algeria) using XRD and FTIR. *Silicon* 9(6): 933-941. https://doi.org/10.1007/s12633-015-9368-6

35. Wei T, Cheng X, Liu H, Zhang H, Zhang L, et al. 2022. Crystallization of tricalcium silicate blended with different silica powder dosages at high temperature. *Constr Build Mater* 316: 125884. https://doi.org/10.1016/j.conbuildmat.2021.125884

36. Chandrasekar A, Sagadevan S, Dakshnamoorthy A. 2013. Synthesis and characterization of nano-hydroxyapatite (n-HAP) using the wet chemical technique. *Int J Phys Sci* 8(32): 1639-1645.

37. Doostmohammadi A, Monshi A, Salehi R, Fathi MH, Seyedjafari E, et al. 2011. Cytotoxicity evaluation of 63s bioactive glass and bone-derived hydroxyapatite particles using human bone-marrow stem cells. *Biomed Pap Med Fac Univ Palacký Olomouc Czech Repub* 155(4), 323-326. https://doi.org/10.5507/bp.2011.028

38. Al-Hamdan RS, Almutairi B, Kattan HF, Alresayes S, Abduljabbar T, et al. 2020. Assessment of hydroxyapatite nanospheres incorporated dentin adhesive. A SEM/EDX, micro-Raman, microtensile and micro-indentation study. *Coatings* 10(12): 1181. https://doi.org/10.3390/coatings10121181